A Trojan horse route to emergent active and stable platinum nanoparticles

Maadhav Kothari[1,†], Yukwon Jeon[1,†], David N. Miller[1], Andrea Eva Pascui[2], John Kilmartin[2], David Wails[2], Silvia Ramos[3], Alan Chadwick[3] and John T.S. Irvine[1*]

[1]School of Chemistry, University of St Andrews, St Andrews, KY16 9ST, U.K.

[2]Johnson Matthey Technology Centre, Sonning Common, Reading, RG4 9NH, U.K.

[3]School of Physical Sciences, Ingram Building, University of Kent, Canterbury, CT2 7NH, U.K.

*Correspondence to: jtsi@st-andrews.ac.uk (Prof. John T.S. Irvine).

†These authors contributed equally to this work.

Platinum demonstrates an exceptional ability as a nanoparticulate catalyst in many important fields, *e.g.* in removing atmospheric pollutants, but it is scarce, expensive and not always sufficiently durable. It is of great importance to develop new highly active and durable supported platinum catalysts to better utilise this critical element. In this study, a perovskite system in which 0.5 wt% of Pt comparable to the industrial standard is strongly integrated into the support to achieve a resilient catalyst is prepared. Due to the difficulty of dissolving Pt into the oxide lattice at high temperature, this was prepared utilising a Barium Platinate Trojan horse via high temperature solid-state synthesis. By tailoring the stoichiometry and reduction procedure, it is possible to produce an equilibrated structure with active emergent Pt nanoparticles that are embedded in the perovskite surface with a uniform distribution and strong support interaction. In doing so, we have created a new catalyst structure with a performance that exceeds that of a conventionally prepared Pt catalyst in CO oxidation activity with greatly improved stability on long-term ageing. After successful labscale testing, the developed perovskite catalyst was evaluated under a variety of reactions at realistic test environments, where CO+NO oxidation, DOC (diesel oxidation catalyst) and ammonia slip reactions were investigated.

Platinum catalysts find widespread use in industry and society. Typically these are dispersed on a porous support, such as γ-Al_2O_3, with low loading of 0.5−2.0 wt% and, for example, have been

extensively used in ECT (Emission control technology) applications in both light and heavy-duty vehicles for the typical four process steps of diesel engines; diesel oxidation, particulate filtration, NO_x reduction and NH_3 slip after treatment (*1,2*). However in automotive catalytic converters, the Pt nanoparticles sinter over time, due to Pt agglomeration and even sublimation at high temperature operation, thus in turn reducing the catalytic activity (*2-4*). This problem has wide reaching effects as older vehicles often emit more particulate matter (PM), CO, NO_x, unburnt hydrocarbons (HC) and even unreacted NH_3 byproduct from NO_x removal. Extending catalytic converter lifetime eases cost concerns on fleet maintenance and minimises loss in performance on prolongd application promoting the future environmental health of urban areas (*5*).

Among many candidates, perovskite materials have received considerable attention both as a supports for platinum group metals and as catalysts themselves (*6, 7*). Previously, a regenerative concept whereby platinum group metal atoms can interchange between metallic nanoparticles and the bulk perovskite matrix to reactivate catalytic activity has been demonstrated by a stoichiometric perovskite system through combustion method at relatively low temperature (*8-10*). However, the low structural phase purity, time frame, movement, support interaction and sporadic dispersion of nanoparticles rendered this ineffective for rapid redox fluctuations common in vehicle engines, resulting in controversy over the mechanism and claims made have raised questions about this approach (*11-13*). Our findings certainly suggest that it is very difficult to homogeneously dissolve Pt into a perovskite structure due to the very limited stability range of Pt oxides, although an overall regenerative process to/from the perovskite matrix clearly occurs with some exchange between Pt and sublattice.

Here, we have designed a fully Pt-incoporated perovskite material from which the resultant emergent Pt nanoparticles are well dispersed and closely integated with the perovskite surface, resulting in excellent catalytic properties. This advance has been achieved by developing an approach based upon the production of emergent first row transition metal nanoparticles from A-site deficient perovskites. This relies upon tailoring the stoichiometry of the initial perovskite

structure so that the B site dopant just emerges from the perovskite structure on reduction. This configuration remains at equilibrium with the support perovskite, resulting in a finely balanced system during high temperature synthesis and highly reducing conditions, yielding well dispersed nanoparticles on the perovskite surface with a strong support interaction, displaying enhanced catalytic performance and sintering resistance (*14-16*). Importantly these particles do not directly re-incorporate into the lattice on re-oxidation. Instead stable, anchored oxide nanoparticles are formed (*15*).

Previous attempts at incorporating Pt into a crystalline perovskite structure have utilised low temperature methods such as combustion synthesis, resulting in low structural clarity and unstable mobile nanoparticles that are more prone to the effects of ageing (*8-13, 17*). Here, we have opted for high temperature solid state synthesis to give better phase purity, which also affords well-characterised materials; however, Pt oxides are unstable, dissociating at low temperatures, ≥400 ^{o}C and so not compatible with solid stae synthesis that usually requires higher temperature (*18).*

To incorporate Pt into an oxide requires stabilising the metal in a high oxidation state and this is best achieved via the use of oxidising atmospheres and especially combination with highly basic oxides such as Ba. Then, it is a matter of using this as a "Trojan horse" precursor to deliver an oxide derivative of Pt and hence to achieve a targetted perovskite composition. $Ba_3Pt_2O_7$, which is capable of withstanding the high temperatures required to form a perovskite phase, *e.g.* up to 1250°C, was synthesized by solid state synthesis (*19*) (Fig. S1). By using such a precursor, it is possible to incorporate Pt ions into the perovskite crystal structure in an O_2-rich environment without the inherent separation of Pt (Fig. 1a). This introduces a small amount of Pt onto the B-site and Ba onto the A-site. Two different A-site deficient perovskite compositions of $La_{0.4}(M)_{0.3925}Ba_{0.0075}Pt_{0.005}Ti_{0.995}O_3$, where M=Ca or Sr were synthesised, incorporating 0.5 wt.% of Pt into the crystal perovskite structure, denoted as **Pt@LCT** or **Pt@LST** (see glossary in SI also), respectively. Fig. 1b and c show SEM (Scanning electron microscope) micrographs of both these surface structures after the perovskite formation. These clearly show clean surfaces with no

nanoparticle decoration or morphological deformity of the crystal structure, similar to the Pt-free analogues (Fig. S2), indicating that Pt is fully incorparated into the crystal structure during a high temperature solid state synthesis

Fig. 1c shows the XRD (X-ray powder diffraction) spectra of **Pt@LCT** and **Pt@LST** with highly crystalline patterns. No visible metallic Pt peak can be observed at 38°-39.8° further indicating the incorporation of Pt into the crystal structure (*3*). The structures with or without Ba and Pt were refined using Rietveld analysis, see extended data Fig. S3 and Table S1. From the perovskite peak shifts in Fig. 1c and the refinement results, tetragonal **Pt@LCT** resides in an *I4/mcm* space group with a smaller primitive unit cell size than cubic **Pt@LST** (*Pm-3m*) due to the difference in cation size between Ca and Sr (Fig. S3e-f). The unit cell parameters show small increases consistent with Pt incorporation (Fig. S3f and Table S1). XAS (X-ray absorption spectroscopy) analysis of the Pt L_{III}-edge in Fig. 1d strongly confirms the incorporation of Pt into the perovskite oxide lattice, with the Pt doped perovskites showing similar XANES (X-ray absorption near edge structure) spectra to the Pt oxides with similar white-line shape and position to PtO_2 and $Ba_3Pt_2O_7$ spectra consistent with Pt^{4+} and obviously different from Pt metal. The EXAFS (Extended X-ray absorption fine structure) show that the Pt environment in the doped perovskite is very different from Pt metal but is close to that in $Ba_3Pt_3O_7$ with Pt in mainly 6-fold coordination (*19*) whilst differing from PtO_2 where Pt is in 3-fold coordination (*20*) which is very different from the coordination expected in a perovskite lattice. Analysis of the structure indicates Pt-O bonding in the oxides and Pt-Pt in the metal.

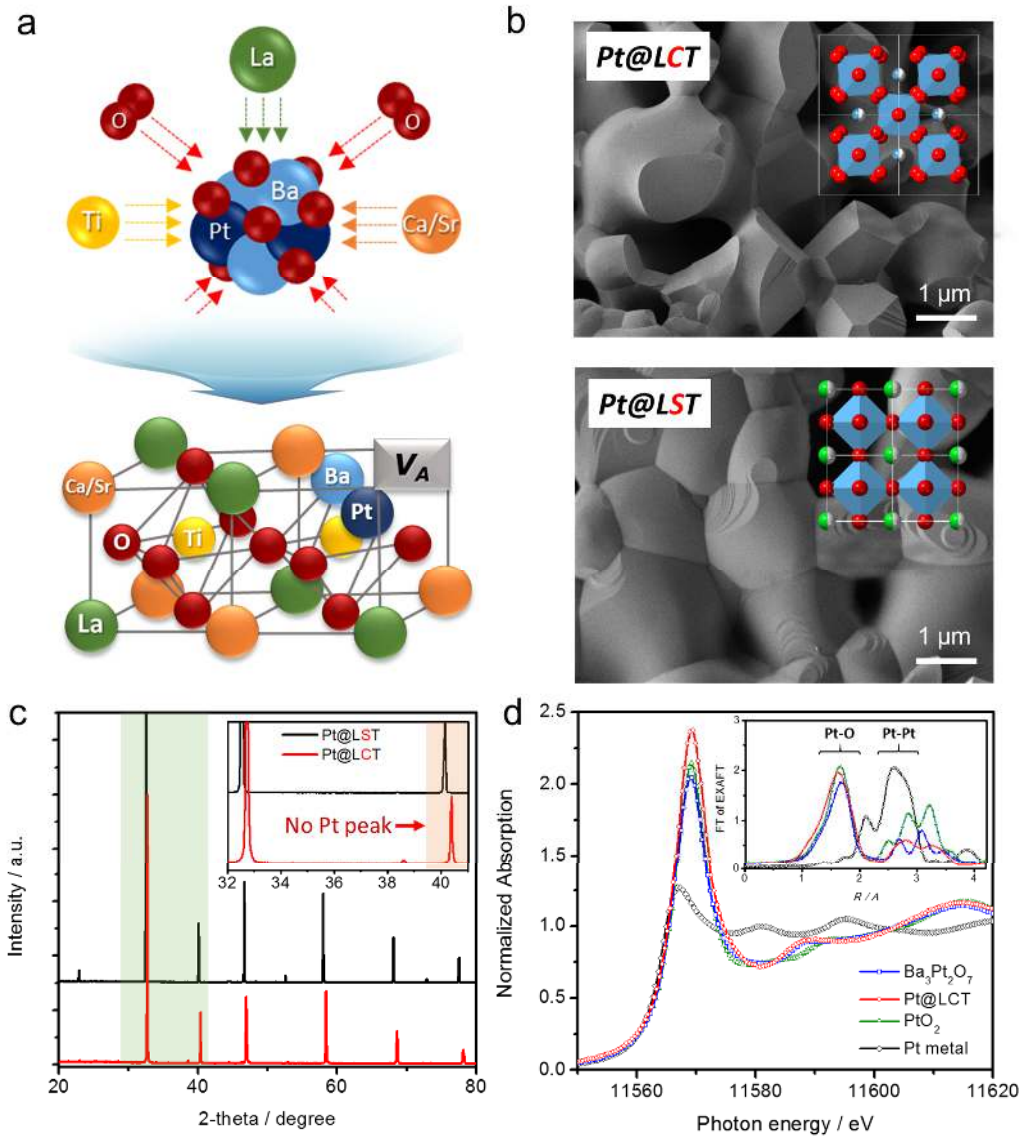

Fig. 1. Characterization of the Pt doped perovskite materials. (a) The illustration of synthesis process of full Pt incorporation into the perovskite structure by using Trojan horse precursor ($Ba_3Pt_2O_7$) and oxidative solid state synthesis conditions. (b) SEM images and (c) XRD patterns (inset: magnification for 32°-42°) for the perovskites of **Pt@LCT** **(**$La_{0.4}Ca_{0.3925}Ba_{0.0075}Pt_{0.005}Ti_{0.995}O_3$) and **Pt@LST** ($La_{0.4}Sr_{0.3925}Ba_{0.0075}Pt_{0.005}Ti_{0.995}O_3$) with Ca form showing Tetragonal splitting as would expected from its analogues. (d) XANES spectra of the Pt L_{III}-edge (inset: EXAFS spectra of the Pt L_{III}-edge) for $Ba_3Pt_2O_7$, **Pt@LCT**, PtO_2 and Pt foil.

The optimum conditions of Pt emergence were guided from TGA (Thermogravimetric analysis) in 5% H_2/Ar. An initial mass step occurred at 700 °C with a total mass loss of 0.42 % on heating to 1000°C and holding for 12 hours (Fig. S4). Pt emergence occured after 700 °C indicating that all Pt (0.5 wt%) was reduced. Further weight loss can be attributed to titanate reduction in the

perovskite. Overall, more O_2 is lost (0.067 atoms per formula unit) than is needed to reduce Pt^{4+} indicating full reduction and emergence of the Pt. 700°C was therefore chosen as reduction temperature, in the assumption that Pt emergence results mainly from the initial reduction step. Applying these conditions, 12 hours at 700°C of reduction, the micrograph in Fig. 2a shows well dispersed Pt nanoparticles decorated on the surface by Pt emergence from A-site deficient **Pt@LCT** and **Pt@LST**, denoted as **Pt+LCT** and **Pt+LST**. Selected regions shown in Fig. 2b-c display morphologically distinct Pt nanoparticles with average size of 15 nm (5-25 nm) and 20 nm (5-35 nm) for **Pt+LCT** and **Pt+LST**, respectively (see Fig. S5). Examination of Fig. 2d-e on the HRTEM (High-resolution transmission electron microscopy) analysis of **Pt+LCT** reveals that the exposed nanoparticles consist of Pt that seem to be embedded into the perovskite surface. From XRD results in Fig. S6, metal Pt peaks are observed for both perovskites without major change in their original perovskite structures indicating the emergence of Pt from the crystal structure. Interestingly, a notable aspect is the difference in Pt emerging tendency between Ca and Sr based perovskites. While the emergent Pt nanoparticles from **Pt+LST** shows pyramidal form with a more localised dispersion, the **Pt+LCT** shows well dispersed spherical Pt nanoparticles across the surface. The different morphological traits could be attributed to a Sr enrichment near the surface as previously observed for Ni containing strontium titanates (*16*). The greater dispersion at **Pt+LCT** is consistent with previous studies indicating more facile emergence for calcium titanate systems (*21*), probably indicating less Ca segregation to the surface. For comparison, impregnated Pt materials ( ) were prepared with the same Pt loading of 0.5 wt% (Fig. S7). Notably, the impregnated **Pt/LCT** in Fig.S7 a-b shows morphological variation and increased size.

The Pt L_{III}-edge XANES spectra of reduced **Pt@LCT** in Fig. 2f confirms the metallic valence state of the emerged Pt nanoparticles from the white-line shape and intensity, with a small difference in amplitude comparing with Pt foil. This might be caused by a morphology effect or by positively charged Pt species from a d-electron density decrease due to the charge transfer of Pt→support, which may result in efficient catalytic properties (*2-4*). The EXAFS analysis in Fig. 2g

also indicates metallic Pt species from the strong contribution from Pt-Pt bonding (~2.7 Å). Remarkably, close examination of Pt-Pt shell for the emerged Pt on **LCT (**$La_{0.4}Ca_{0.4}TiO_3$) reveals a high reduction in the intensity, compared to the impregnated Pt comparators. The reduced amplitude links to the reduction of the average coordination number of 12 for the Pt-Pt bonding in the Pt metal bulk. From the refined analysis in Fig. S8 and Table S2, the Debye-Waller factor (σ^2) increases with a reduction of the interatomic distance (R), suggesting a strong structural disodering of the emerged Pt. Both observations are consistant with a strong interaction between the Pt nanoparticles and perovskite bulk, which could contribute to the stabilization of the Pt nanoparticles in sintering conditions.

< Place in two columns>

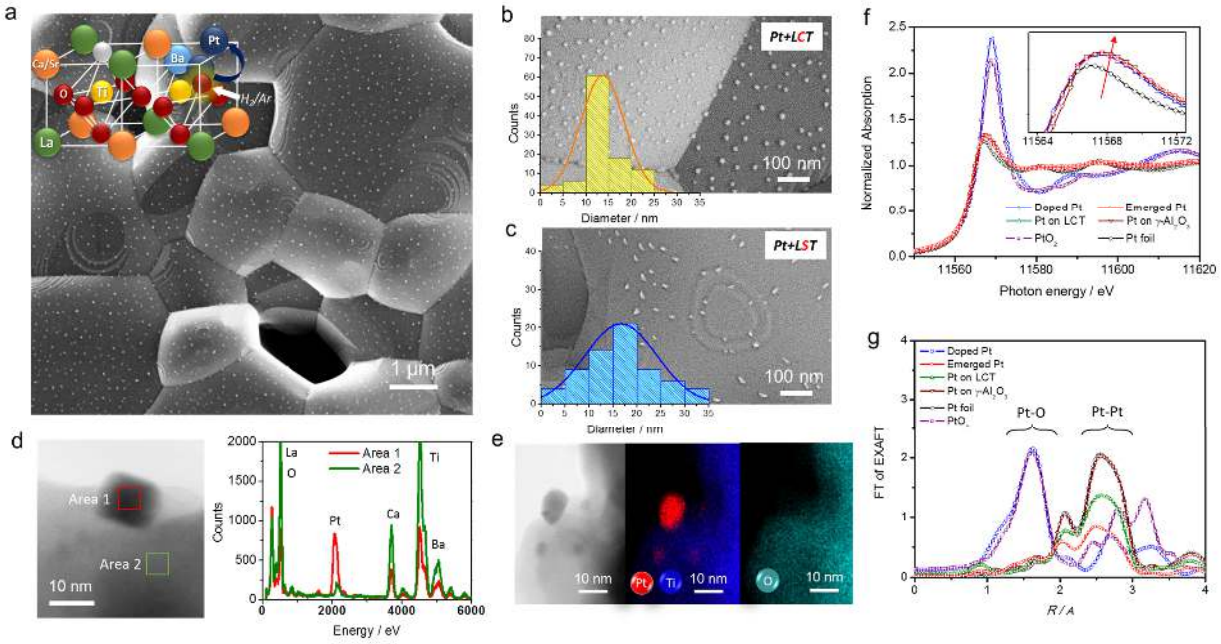

Fig. 2. Emergent Pt Nanoparticles from the tailored perovskite materials. (a) SEM image (inset: illustration of the proposed emergence mechanism) of the emerged Pt perovskites for (b) **Pt+LCT** and (c) **Pt+LST** with each Pt nanoparticles size distributions. TEM images with the EDX (d) spot and (e) mapping analysis of the emerged Pt perovskites. (f) XANES and (g) EXAFS spectra of the Pt L_{III}-edge for the **Pt@LCT, Pt+LCT**, **Pt/LCT**, **Pt/γ-Al_2O_3**, PtO_2 and Pt foil.

Catalytic performance of all samples was initially tested for CO oxidation at lab-scale conditions as shown in Fig. 3a. Non-doped perovskite demonstrated almost no catalytic activity, while an increased activity was observed after Pt incorporation prior to reduction. As expected, a very significant increase in catalytic performance was obtained after emergence of the Pt nanoparticles in both samples. While perovskites with Ca or Sr showed a difference in catalytic activity due to the difference in Pt nanoparticle morphology and distribution, emergent **Pt+LCT** exhibited a superior performance with a light-off curve at 190 ^{o}C for 100 % CO conversion at low Pt loading of 0.5 wt.%, compared to impregnated **Pt/LCT** (240 ^{o}C). Remarkably, the activity was even higher than the commercial type **Pt/γ-Al_2O_3** (220 ^{o}C), with 20% higher CO oxidation activity at 190^{o}C, despite a low surface area (1-2 m^2/g) compared to **Pt/γ-Al_2O_3** (112.7 m^2/g) as in Fig. S6. Another interesting result was that Pt+LCT also retained good oxidation activity in partial O_2 environment (Fig. S9a), maintaining activity with 50% oxygen partial pressure and outperforming **Pt/Al_2O_3** at 1:1 (CO:O_2). XPS O 1s (Fig. S9b-d) showed that the perovskite surface possesses a large portion of active oxygen (O_D+O_C) species (*4, 22*), resulting in oxygen sites that are involved more in oxidation reactions rather than O_L. These were further increased, especially O_D through the Pt emergence. These observations confirm an efficient oxidation mechanism (Fig. 3a) at the uniquely active Pt species and possession of active oxygens that are important factors for the outstanding catalytic performance.

To explore the stability of **Pt+LCT**, aging tests were performed in Fig. 3b at 800 ^{o}C and air for more than 2 weeks (350 hrs, see Table S4 aging 1). The reactivity of **Pt+LCT** did not change compared to that of the fresh catalyst, which satisfies the requirements of the general accelerated aging set in DOCs (*3, 4, 23*). In contrast, impregnated **Pt/LCT** and **Pt/γ-Al_2O_3** showed typical ageing behaviour, in which the activity drops significantly, interestingly both follow the same shift in light off to a higher temperature. Severe Pt agglomeration of impregnated **Pt/LCT** and **Pt/γ-Al_2O_3** was observed with variation in morphology, size and shape (Fig. S10, S11). Notably, 350 hour aged **Pt+LCT** (Fig. 3c) retains an average Pt nanoparticle size of 15 nm with an even

distribution on the surface, indicating remarkable sintering resistance due to the embedded nature and strong metal-perovskite interaction despite some noticeable re-ordering of the perovskite surface itself. Aging tests were carried on all these materials and reaction conditions, with Pt+LCT showing superior catalytic activity after all the ageing protocols detailed in table S4.

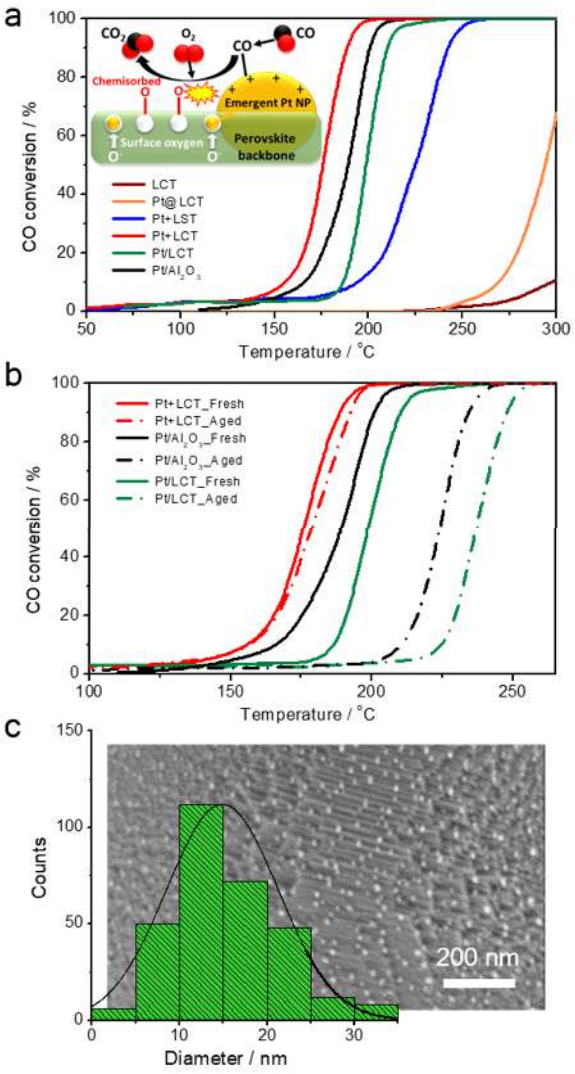

Figure 3. Catalytic functionality for CO oxidation at the perovskite catalysts with emergent Pt Nanoparticles. (a) Light-off curves for initial CO oxidation for a feed mixture gas of 20,000 ppm CO, 10.0 vol.% O_2 from air (21% O_2 and 79% N_2) at N_2 balance with a total gas flow rate of 200 ml/min (GHSV=60,000/hr) on the prepared samples. (inset: reaction mechanism of **Pt+LCT**) (b) Light-off curves for CO oxidation before and after and in-situ aging at 800 °C under an air gas flow of 50 ml/min for over 2 weeks (350 hrs, see table S4 aging 1) for emergent **Pt+LCT**, infiltrated **Pt/LCT** and **Pt/γ-Al_2O_3**. (c) SEM image with the Pt Nanoparticles distribution after the 350 hour aging test of **Pt+LCT**.

The materials were further tested in a variety of reactions to an appropriate industrial standard in accordance with in house pre-screening process of novel catalysts for CO and NO

removal (see Fig. S12), diesel oxidation catalyst (DOC) conditions and an ammonia oxidation catalyst (AMOX) (see Fig. S13) to address slip to demonstrate capability for practical ECT applications in simulated real car exhaust environments (eg see aged samples Fig S14). Particularly, the results of NO removal reaction driven by CO were collected using feed streams of CO and NO with comparable stoichiometries and GHSV to that observed in simulated car exhausts. It was found that the developed catalyst is highly effective for NO conversion driven by the presence of CO, as illustrated in Fig. 4a. Even under high GHSV (gas hourly space velocity) conditions, the CO reduction activity of the materials followed the same trend in the light-off plots as those observed at the initial CO oxidation tests supported by the perovskite's oxygen storage capacity (Fig. S4). Interestingly, the NO conversion also reached a relatively high value of over 80 % at 450 ^{o}C for emergent **Pt+LCT** compared to infiltrated **Pt/LCT** (35 %) and **Pt/γ-Al_2O_3** (63 %), which suggests a possible reaction scheme (Fig. 4a) due to the synergistic effect at highly distributed active Pt nanoparticles and available oxygens at the perovskite surfaces.

These properties are reflected well in the DOC (C_3H_6, CO and NO) and AMOX (NH_3 and CO) reaction tests containing O_2, H_2O and CO_2, with model automotive exhaust gas compositions, with stability well illustrated in fig. S14. In modern diesel engine after treatment systems, DOCs are functioned to oxidize the exhaust gases to harmless products, also NO to support the performance of diesel particulate filters and SCR catalysts. From Fig. 4b, **Pt+LCT** shows a strong ability in catalysing propylene (C_3H_6) oxidation at low temperature (260 ^{o}C) while simultaneous multiple oxidations are observed. The mixing of the feed gases marginally lowered the NO conversion, suggesting that CO and C_3H_6 oxidations take place preferentially. However, when we compare each reaction to **Pt/γ-Al_2O_3**, all the results were improved by at least 20 % in each conversion. In the case of ammonia slip, there is an automotive industrial problem whereby the excess NH_3 from some NOx removal processes is emitted into the atmosphere. In order to mitigate the excess NH_3, currently 0.5-1% **Pt/γ-Al_2O_3** catalysts are used within AMOX catalyst systems so this is a useful comparator. As seen from Fig. 4c, **Pt+LCT** shows a lower onset temperature (230 ^{o}C) for 100%

NH_3 oxidation compared to **Pt/γ-Al_2O_3** (245 °C), where the accompanying CO oxidation also gives 100 % CO conversion. These both confirm great catalytic ability of the emergent **Pt+LCT** catalyst for multiple oxidations for not only light gases like CO and NO, but also harmful hydrocarbons and even excess NH_3.

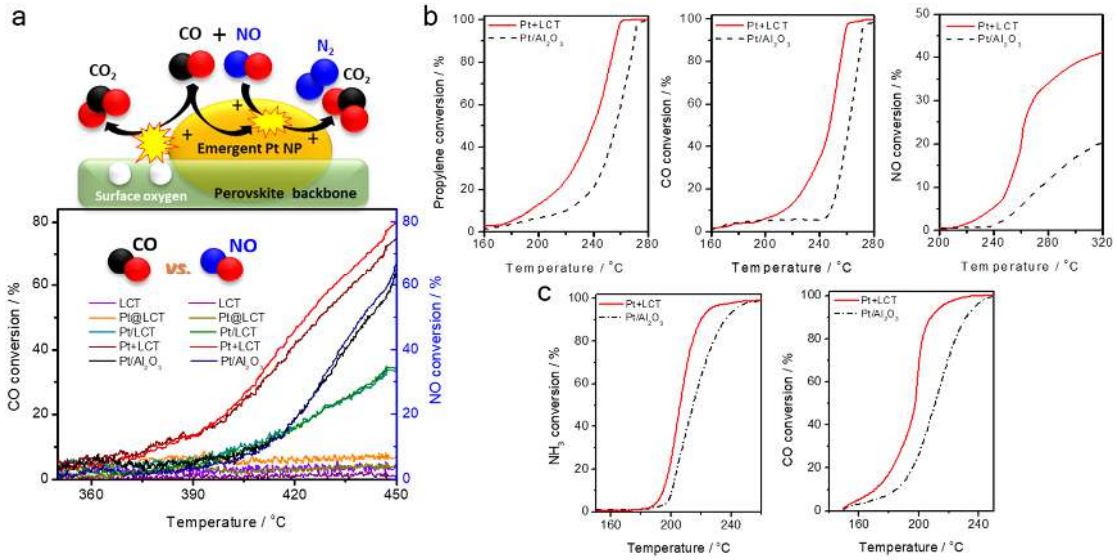

Figure 4. Catalyst performance under the simulated car exhaust environments. (a) reaction mechanism of **Pt+LCT** and results in a mixture of 4,000 ppm CO and 4,000 ppm NO at stoichiometric conditions in feed streams and an GHSV level of real car exhausts, calculated from the raw data in Fig. S12. (b) DOC (C_3H_6 and CO+NO in feed streams) and (c) AMOX (NH_3 and CO in feed streams) test results of each reactants in the presence of O_2 (10%), H_2O (5%) and CO_2 (4.5%) for emergent **Pt+LCT** and **Pt/γ-Al_2O_3**, obtained from the raw data in Fig. S13.

In conclusion, we demonstrate a new approach of using a Trojan horse precursor to synthesise a perovskite with excellent integration of Pt into the oxide lattice via high temperature solid state reaction, which can also be applied to other metals and alloys that are unstable as metal oxides at perovskite synthesis temperatures and in fact these are often the most exciting candidate metal nanocatalysts Catalytically active and robust emergent Pt nanoparticles anchored on the surface were produced, yielding a highly catalytically active configuration, which was immune to the typical effects of agglomeration through a strong interaction with the bulk perovskite structure,

demonstrating great potential for use in wide variety of industrially relevant catalytic reaction systems.

References and Notes:

1. R. J. Farrauto, Low-Temperature Oxidation of Methane. *Science* **337**, 659-660 (2012)
2. Z. Zhang, Y. Zhu, H. Asakura, B. Zhang, J. Zhang, M. Zhou, Y. Han, T. Tanaka, A. Wang, T. Zhang, N. Yan, Thermally stable single atom Pt/m-Al2O3 for selective hydrogenation and CO oxidation. *Nat. Comm.* **8**, 16100 (2017).
3. J. Jones, H. Xiong, A. T. DeLaRiva, E. J. Peterson, H. Pham, S. R. Challa, G. Qi, S. Oh, M. H. Wiebenga, X. I. P. Hernández, Y. Wang, A. K. Datye, Thermally stable single-atom platinum-on-ceria catalysts via atom trapping. *Science* **353**, 150–154 (2016).
4. L. Nie, D. Mei, H. Xiong, B. Peng, Z. Ren, X. I. Pereira Hernandez, A. DeLaRiva, M. Wang, M. H. Engelhard, L. Kovarik, A. K. Datye, Y. Wang, Activation of surface lattice oxygen in single-atom Pt/CeO2 for low-temperature CO oxidation. *Science* 358, 1419–1423 (2017).
5. S. L. Winkler, J. E. Anderson, L. Garza, W. C. Ruona, R. Vogt, T. J. Wallington, Vehicle criteria pollutant (PM, NOx, CO, HCs) emissions: how low should we go?. *npj Climate and Atmospheric Science* **1**, 26 (2018).
6. J. Hwang, R. R. Rao, L. Giordano, Y. Katayama, Y. Yu, Y. Shao-Horn, Perovskites in catalysis and electrocatalysis. *Science* **358**, 751–756 (2017).
7. C. H. Kim, G. Qi, K. Dahlberg, W. Li, Strontium-Doped Perovskites Rival. *Science* **327**, 1624–1627 (2010).
8. H. Tanaka, M. Taniguchi, M. Uenishi, N. Kajita, I. Tan, Self-Regenerating Rh-and Pt-Based Perovskite Catalysts for Automotive-Emissions Control. *Angew. Chemie* **45**, 5998–6002 (2006).
9. I. Jarrige, K. Ishii, D. Matsumura, Y. Nishihata, M. Yoshida, H. Kishi, M. Taniguchi, M. Uenishi, H. Tanaka, H. Kasai, J. Mizuki, Toward optimizing the performance of self-regenerating Pt-based perovskite catalysts. *ACS Catal.* **5**, 1112–1118 (2015).
10. Y. Nishihata, J. Mizuki, T. Akao, H. Tanaka, M. Uenishi, M. Kimura, T. Okamoto, N. Hamada, Self-regeneration of a Pd-perovskite catalyst for automotive emissions control. *Nature* **418**, 164–167 (2002).
11. S. Zhang, M. B. Katz, S. Dai, K. Zhang, X. Du, G. W. Graham, X. Pan, New Atomic-Scale Insight into Self-Regeneration of Pt-CaTiO3Catalysts: Incipient Redox-Induced Structures Revealed by a Small-Angle Tilting STEM Technique. *J. Phys. Chem. C* **121**, 17348–17353 (2017).
12. S. A. Malamis, R. J. Harrington, M. B. Katz, D. S. Koerschner, S. Zhang, Y. Cheng, L. Xu, H.-W. Jen, R. W. McCabe, G. W. Graham, X. Pan, Comparison of precious metal doped and impregnated perovskite oxides for TWC application. *Catal. Today* **258**, 535–542 (2015).
13. M. B. Katz, G. W. Graham, Y. Duan, H. Liu, C. Adamo, D. G. Schlom, X. Pan, Self-regeneration of Pd-LaFeO3 catalysts: New insight from atomic-resolution electron microscopy. *J. Am. Chem. Soc.* **133**, 18090–18093 (2011).
14. D. Neagu, G. Tsekouras, D. N. Miller, H. Ménard, J. T. S. Irvine, In situ growth of nanoparticles through control of non-stoichiometry. *Nat. Chem.* **5**, 916–923 (2013).

15. D. Neagu, E. I. Papaioannou, W. K. W. Ramli, D. N. Miller, B. J. Murdoch, H. Ménard, A. Umar, A. J. Barlow, P. J. Cumpson, J. T. S. Irvine, I. S. Metcalfe, Demonstration of chemistry at a point through restructuring and catalytic activation at anchored nanoparticles, *Nat. Comm.* **8**, 1855 (2017).
16. D. Neagu, T.-S. Oh, D. N. Miller, H. Ménard, S. M. Bukhari, S. R. Gamble, R. J. Gorte, J. M. Vohs, J. T. S. Irvine, Nano-socketed nickel particles with enhanced coking resistance grown in situ by redox exsolution. *Nat. Comm.* 6, 8120 (2015).
17. Y. Gao, J. Wang, Y.-Q. Lyu, K. Lam, F. Ciucci, In situ growth of Pt3 Ni nanoparticles on an A-site deficient perovskite with enhanced activity for the oxygen reduction reaction. *J. Mater. Chem. A* **5**, 6399–6404 (2017).
18. A. S. M. Nur, E. Funada, S. Kiritoshi, A. Matsumoto, R. Kakei, S. Hinokuma, H. Yoshida, M. Machida, Phase-Dependent Formation of Coherent Interface Structure between PtO2 and TiO2 and Its Impact on Thermal Decomposition Behavior. J. Phys. Chem. C **122**, 662–669 (2018).
19. P. S. Haradem, B. L. Chamberland, L. Katz, A. Gleizes, A structural model for barium platinum oxide, Ba3Pt2O7. *J. Solid State Chem.* **21**, 217–223 (1977).
20. Prabha, I. Current Status of Platinum Based Nanoparticles : Physicochemical Properties and Selected Applications – A Review. 122–133 (2019).
21. J-H. Myung, D. Neagu, D.N. Miller & JTS. Irvine, Switching on electrocatalytic activity in solid oxide cells, *Nature,* **537**, 528–531 (2016).
22. Y. Jeon, D.-H. Park, J.-I. Park, S.-H. Yoon, I. Mochida, J.-H. Choy, Y.-G. Shul, Hollow Fibers Networked with Perovskite Nanoparticles for H2 Production from Heavy Oil. *Sci. Rep.* **3**, 2902 (2013).
23. U.S. D.R.I.V.E. Partnership, "After treatment Protocols for Catalyst Characterization and Performance Evaluation: Low-Temperature Oxidation Catalyst Test Protocol (2015; https://cleers.org/wp-content/uploads/2015_LTAT-Oxidation-Catalyst-Characterization-Protocol.pdf).
24. Z. Zhang, G. R. Lumpkin, C. J. Howard, K. S. Knight, K. R. Whittle, K. Osaka, Structures and phase diagram for the system CaTiO3-La2/3TiO3. *J. Solid State Chem.* **180,** 1083–1092 (2007).

Dedication: We would like to dedicate this work to our esteemed co-author and colleague, David Wails, who tragically died in Reading on 20th June 2020

Acknowledgments: We acknowledge useful discussions with Martin Fowles and Janet Fisher from Johnson Matthey. We thank the Diamond Light Source for the award of beam time as part of the Energy Materials Block Allocation Group SP14239; **Funding:** Johnson Matthey and EPSRC for a CASE PhD studentship, EPSRC for a Critical Mass project EP/R023522/1 and Electron Microscopy provision EP/R023751/1, EP/L017008/1; **Author contributions:** M. K. and Y. K. J. designed and carried out the experiments, and wrote the manuscript. D.N.M. collected TEM and EDX data. S. R. and A. C. analyzed the XANES/EXAFS results. A. P. and J. K. carried out the conventional catalyst tests in Johnson Matthey and D. W. and J. F. analyzed the results. J.T.S.I. supervised the whole study and revised the manuscript. All authors discussed the results and commented on the manuscript.; **Competing interests:** Authors declare no competing interests.; and **Data and materials availability:** All underlying data is available on the St Andrews PURE website at DOI: tbc

Materials and Methods

Precursors.

High purity oxide and carbonate precursors, such as La_2O_3 (Pi-Kem, >99.99%) and TiO_2 (Alfa Aesar, >99.6%), $BaCO_3$ (Alfa Aesar, >99%), $CaCO_3$ (Fisher Chemical, >99%) and $SrCO_3$ (Aldrich, >99.9%), are dried at 300 ºC (La_2O_3 at 800 ºC) in order to remove water bound molecules from the precursors for a correct stoichiometric nature of the perovskites. PtO_2 (Alfa Aesar, anhydrous) and Pt nitrate solution (Johnson Matthey, 16.17 wt% Pt) are used as Pt precursors, and γ−Al_2O_3 (Sasol, Particle size ≤ 5 mm, S_{BET} 138−158 m^2/g) is purchased.

Trojan horse co-precursor $Ba_3Pt_2O_7$.
$BaCO_3$ and PtO_2 are weighed and mixed together in the correct stoichiometric amount in a Pt crucible, and then fired in air in a furnace with a ramp rate of 5 ºC/min to 1000°C for 12 hrs.

Pt doped Perovskite synthesis.
A-site deficient perovskites of $La_{0.4}Ca_{0.3925}Ba_{0.0075}Pt_{0.005}Ti_{0.995}O_3$ (**Pt@LCT**) and $La_{0.4}Sr_{0.3925}Ba_{0.0075}Pt_{0.005}Ti_{0.995}O_3$ (**Pt@LST**) are designed by containing 0.5 wt% of Pt. Non-doped perovskites of $La_{0.4}Ca_{0.4}TiO_3$, $La_{0.4}Sr_{0.4}TiO_3$, $La_{0.4}Ca_{0.3925}Ba_{0.0075}TiO_3$, and $La_{0.4}Sr_{0.3925}Ba_{0.0075}TiO_3$ are prepared as references. Carefully calculated precursor quantities are quantitatively transferred to a glass beaker, then acetone is added to the beaker with a co-polymer dispersant (Hypermer KD-1, a polyester copolymer surfactant). The mixture is pulse sonicated using an ultrasonic probe (Heilscher UP200S) in order to homogenise and reduce the particle size of the precursors. Following dispersion, acetone is evaporated from the homogeneous solution and the compositional mixture is then calcined in a muffle furnace at 1000 ºC for 12 hrs to partially form the perovskite phase for seeding crystallisation. Following calcination, the sample is ball milled with acetone at 300 rpm for 2 hrs in a planetary ball mill, using 1 mm zirconia balls. Then, the sample is dried in an evaporator dish at room temperature.

O_2-rich sintering process.
Pellets are prepared by pressing the sample powders and then firing them under O_2-rich sintering conditions to produce pure perovskite phase at the relatively low temperatures. Pellets are fired for 12 hrs at 1200 ºC with a ramp rate of 5 ºC/min in an O_2-rich gas atmosphere of 100% O_2 and 100 $ml \cdot min^{-1}$.

In-situ emergence process.
To emerge the Pt NPs onto the perovskite surface, samples are chemically reduced in a controlled atmosphere furnace at 700 ºC for 12 hrs with heating and cooling rates of 5 °C·min^{-1} under continuous flow of 5% H_2/Ar (20 $ml \cdot min^{-1}$). The emerged Pt perovskites are denoted as **Pt+LCT** and **Pt+LST**.

Reference samples.
For a comparison, Pt impregnated LCT (**Pt/LCT**) and **Pt/γ−Al_2O_3** catalysts are synthesized by the incipient wetness method. Constant Pt concentration of 0.5 wt% was impregnated to the supports by a Pt nitrate solution, then dried at 110 °C for 24 hrs and calcined at 550 °C for 3 hrs in air. The **Pt/LCT** and **Pt/γ−Al_2O_3** samples are reduced in 5% H_2/Ar flow for 12 hrs at 700 ºC and 500 ºC, respectively.

X-ray Powder Diffraction (XRD).
XRD measurements are carried out at room temperature with an x-ray angle from 10-90º by using a PAN analytical Empyrean diffractometer with CuKα1 radiation (1.54056Å) and Bragg-Brentanon geometry operated in reflection mode. STOE Win XPOW software is used to analyze the diffraction pattern and interoperate the crystal structure and cell parameter. GSAS open source refinement software is applied for carrying out Rietveld refinement of the results to find out the

original perovskite phase and structural changes. The structural information is then used to construct the crystal structure by using Crystal Maker for Windows software.

X-ray absorption spectra (XAS).

The X-ray absorption near edge structure (XANES) and extended X-ray absorption fine structure (EXAFS) of the Pt L_{III}-edge for selected samples are collected at ambient temperature, on the B18 station at Diamond Light Source national synchrotron facility, UK. Measurements are carried out using a Si(111) monochromator at Pt L_{III}-edge with a Pt monometallic foil (10 μm) used as an energy calibrant. Samples are pressed into 13 mm pellets, and high Pt loaded samples are diluted using appropriate amount of cellulose binder. Pt foil and PtO_2 are used as references for Pt^0 and Pt^{4+}, respectively. XAS data analysis was carried out with the software of Athena and Artemis (*2*).

EXAFS fitting

The EXAFS functions were Fourier transformed in the *k* range of 3–13.86 $Å^{-1}$ and multiplied by a Hanning window. The basic structural model was a (fcc) Pt metal core from the ICSD code of 243678. The structure refinement was carried out using ARTEMIS software (IFFEFIT) (*2*). Moreover, the theoretical backscattering amplitudes and phases were calculated by FEFF 6.0. Then, the theoretical data corresponding to the first Pt–Pt shell were adjusted to the experimental spectra by a least square method in R-space from 1.8 to 3.12 Å. The amplitude reduction factors (S_0^2) were calculated using Pt foil model, based on the coordination number (*N*) of 12. The other fitting parameters were σ^2 (Debye-Waller factor: mean square deviation of interatomic distances), *R* (Average interatomic distance, R_{eff}: 2.77410 for Pt-Pt), ΔE0 (Energy shifts: inner potential correction between the samples and the FEFF calculation). The R-factor represents the absolute misfit allowed for the data range that were fittined between theory and experiment. The number of the independent points according to the Nyquist criterion was 8.86 and the number of the fitting parameters was 4.

Scanning electron microscope (SEM) and particle tracking.

FEI Scios electron microscope equipped with secondary and backscattered electron detector is used to acquire high-resolution images for investigating surface morphology and phase homogeneity, especially the Pt NPs distributed on the sample surfaces. To track the Pt NPs, the number and size on the surfaces are calculated for particle size distribution histograms from the adequately magnified images using Image-Pro Plus software. The selected SEM images are converted to binary images where particles are distinguished by the pixel contrast. Particle sizes are calculated by a calibration of the SEM image scale between pixel and nm, where the particles are assumed to be a hemispheric.

High-resolution transmission electron microscopy (HR-TEM).

To analyse more in detail about the morphological and elementary study on the Pt on the sample, HR-TEM imaging is carried out by the FEI Titan Themis instrument, using a 25 keV He^+ beam with 0.2 pA beam current. The elementary study through the energy dispersive X-ray (EDX) are also performed by spot and mapping analysis to distinguish the Pt NPs on the sample surface compare to the desired perovskite compositions (La, Ca, Ba, Pt, Ti, and O).

Thermogravimetric analysis (TGA).

TGA measurements are carried out on a NETZSCH STA 449 C instrument using Proteus thermal analysis software. The initial weight of the sample is about 20 mg. The buoyancy effect is corrected using empty crucible blank runs under corresponding chemical reduction gas atmosphere of flowing 5% H_2/Ar (30 ml/min). First, the sample is heated up to 1000 °C with a heating rate of 5 °C min^{-1}. Second, the sample is heated up to 700 °C with a heating rate of 5 °C min^{-1} and kept for 15 hrs.

N_2 isothermal analysis. Specific surface area (S_{BET}), average pore volume and pore size of the prepared samples are determined by the distribution graph of N_2 adsorption-desorption at 77 K using Micromeritics TRISTAR II 3020. Samples are outgassed at 150 °C under vacuum for 12 hr using a Quantachrome Flovac degasser (Micromeritics VacPrep 061). N_2 isothermal data set were collected at -195 °C. S_{BET} is calculated by the Brunauer-Emmett-Teller multiple point method at partial pressure range from 0.05 to 0.3. Total pore volume is determined at p/p_0=0.99.

X-ray photoelectron spectroscopy (XPS).
The O 1s XPS spectra are collected by thermo Scientific K-Alpha instrument equipped with monochromatic Al X-ray source (Al Kα, 1486.6 eV), using a hemispherical energy analyzer. The samples are fixed on carbon tape and all binding energies are calibrated using C 1s (284.8 eV). The results are analysed and fitted using Fityk software by a linear type background subtraction and appropriate curve shape fitting.

Initial lab-scale tests on catalytic CO oxidation and stability aging.
The catalytic performances of as-synthesized samples for CO oxidation are evaluated in a laboratory scale fixed–bed quartz reactor (internal d8 mm) under atmospheric pressure. The temperature is controlled by the K-type thermocouple at the centre of the reaction zone and gas flows are controlled by the electronic mass-flow controllers (MFC, ALICAT scientific). Approximately 200 mg of samples are ground and sieved to 40-60 mesh to load into the reactor by quartz wool at each side. The samples are pre-treated in-situ with 5% H_2/Ar at 300 °C for 1 hr, and then purged with N_2 for 30 min to remove the residual H_2. After cooling to 70 °C, a feed mixture gas of 20,000 ppm CO, 10.0 vol.% O_2 from air (21% O_2 and 79% N_2) at N_2 balance is introduced with a total gas flow rate of 200 ml·min^{-1} (GHSV=60,000/hr). The light-off experiments are measured at the range of 70-300 °C with a ramp rate of 3 °C·min^{-1}, sampling performed every 10 °C. At a fixed CO concentration and GHSV, the oxygen partial pressures for CO oxidation reaction are varied by 1, 5 and 10 vol.% O_2 from air (21% O_2 and 79% N_2). The composition of the effluent gas products is measured by on-line TCD gas chromatography (GC-2014, SHIMADZU) equipped with a molecular sieve 5A (60-80 mesh) column. The CO conversion is calculated by the change of the CO concentrations. In-situ aging tests for the initially tested catalysts are performed at 800 °C under an air gas flow of 50 ml·min^{-1} for over 2 weeks (around 350 hrs). The aged samples are then re-run through light-off experiments at same reaction conditions. Post-characterizations of the aged samples are carried out by SEM analysis and particle tracking.

Simulated car exhaust conditions.

To evaluate the catalysts in realistic environments, CO+NO, diesel oxidation and ammonia slip reactions are tested. CO+NO model reaction was designed to evaluate the materials for the three-way catalytic converters. The tests were carried out in a temperature-programmed fixed-bed reactor by ramping up the temperature from 90 °C to 500 °C at a rate of 10 °C/min and using 0.2 g of catalyst mixed with 0.2 g of cordierite. The inlet concentrations were fixed to the concentrations of 4000 ppm CO and 4000 ppm NO, respectively, at a total flow of 12 L/min at N_2 balance. DOC (Diesel oxidation catalyst) model reaction was used to evaluate the use of the materials for real automotive catalytic converters. The tests were carried out in a steady state temperature-programmed reactor at the temperature range of 150 °C to 330 °C with a 10 min hold at each temperature stages. The total flow was 12 L/min at N_2 balance with the gas composition of 1450 ppm CO, 105 ppm propylene (C_3H_6), 125 ppm NO, and 4.5% CO_2, 10% O_2 and 5% H_2O (steam). Ammonia slip model reaction is to evaluate the possibility on removing excess NH_3 from the non-catalyzed NH_3. A steady state temperature-programmed reactions was carried out from 150 °C up to 330 °C with a 10 min hold at each temperature stages. Inlet conditions were 550 ppm NH_3, CO 220 ppm with 4.5% CO_2, 10% O_2 and 5% H_2O (steam) at the N_2 balanced total flow of 12 L/min. For the gas products analysis on each reaction, both inlet and outlet gases were measured by MKS

MG2000 multi-gas analyser using a FT-IR detector. The conversions are calculated by the change of each gas concentrations and the light-off curves were plotted from the conversion values at each temperature stages